Customizing the structure and chemical composition of ultralight carbon foams for superior microwave absorption performance

Tingting Cheng
Qingdao University of Science and Technology

Yuying Guo
Qingdao University of Science and Technology

Yuxin Xie
Qingdao University of Science and Technology

Laibin Zhao
Qingdao University of Science and Technology

Ting Wang
Qingdao University of Science and Technology

Alan Meng
Qingdao University of Science and Technology

Zhenjiang Li (✉ zhenjiangli@qust.edu.cn)
Qingdao University of Science and Technology

Meng Zhang
Qingdao University of Science and Technology

Research Article

Abstract

Developing biomass-derived three-dimensional porous carbon materials (porous carbon foam, PCF) has become a common strategy to obtain lightweight and efficient electromagnetic microwave-absorbing materials. Without the introduction of a template and subsequent activation process, several ultra-lightweight honeycomb PCF samples were successfully prepared from dried ballonflower (DB) by simple calcination, and the calcination temperature plays a decisive role in regulating the pore size, composition and microwave absorption properties of PCF samples. Furthermore, it is worth noting that different cutting directions also affected the hole size of the PCF sample as well as the microwave absorption performances. Under the combined effects of multiple reflections and scattering of PCF porous structure, dipole polarization of abundant heterogeneous atoms and good conductive loss of carbon material, the vertical cutting sample PCF-900V exhibits optimal microwave absorption performances with the minimal reflection loss (RL_{min}) value of -46.95 dB at 1.46 mm thickness and the effective absorption bandwidth (EAB) value of 5.52 GHz at 1.72 mm matching thickness respectively, indicating its great potential application as a promising lightweight and efficient microwave absorbing material.

1 Introduction

With the development and popularity of various new electronic devices, a source of pollution known as the "invisible killer"-electromagnetic radiation, has caused an increasingly severe impact on humans and the environment and gradually the attention of society [1−5]. Previous studies have pointed out that long-term exposure to high-intensity electromagnetic radiation may seriously damage the human central nervous system, immune system, cardiovascular system and visual system, even threatening the health of a woman's fetus during pregnancy [6−9]. Therefore, developing a suitable microwave absorbing material to cope with the increasingly severe electromagnetic pollution problem has become an important research topic in materials science.

With the portability and integration of various electronic devices, the industry has put forward more comprehensive performance requirements for future wave-absorbing materials to match them, including low density, small thickness, wide frequency range, and strong wave absorption ability [10]. Undoubtedly, carbon-based microwave-absorbing materials with low density, high stability [11], high electrical conductivity, and wide variety have become the first choice for researchers [12−15].

Biomass-derived three-dimensional (3D) [16] porous carbon can be regarded as a bulk carbon with a large number of pore structures, i.e. a composite material composed of bulk carbon and pore structures, which can be adjusted to effectively regulate its microwave absorption performance [17], which is not possible for bulk carbon materials. From the process point of view, biomass-derived three-dimensional porous carbon also has the advantages of a wide range of raw materials, environmentally friendly [18], simple production process, low cost and can be produced on a large scale [19], which can better meet the practical requirements of the industry for microwave absorbing materials [20−22].

To date, researchers have carried out a lot of exploratory work in tuning the structure of bio-derived 3D porous carbon to enhance microwave absorption performance [23–25]. They have achieved some promising results, while some unavoidable problems need to be solved. Firstly, it is difficult to adjust the pore size of the woody plant-derived carbon because they inherit the native pore structure of the precursor feedstock well during the carbonization process. Secondly, strong acids or bases are usually used to etch/activate biomass-derived carbon to improve porosity, which does not meet the standards of the green chemical industry. More importantly, the currently reported methods for adjusting the structure of the derived carbon pores are accompanied by the change of the composition and functional group content of the products, which affects the dipole polarization [26] for the incident electromagnetic waves. It also hindered us from identifying the relationship between the cavity size of the sample and the corresponding electromagnetic wave absorption performances. Therefore, it has become a consensus for researchers to obtain high porosity biomass-derived carbon with adjustable size through a simple preparation process and to grasp the law of the influence of pore structure on the absorbing properties of the products.

In this work, employing a novel biomass (DB) raw material, an ultra-lightweight porous derived carbon foam (PCF) was prepared via a simple calcination process. Besides exploring the influence of calcination temperature on the hole size, composition, and microwave absorption properties, the relationship between cutting direction and microwave absorption performances was first investigated systematically. The outstanding absorption performances suggest that the PCF sample can be served as a promising lightweight absorbing material. This environmentally friendly preparation process may have important implications for constructing novel lightweight magnetic carbon-based absorbing material.

2 Experimental Section

2.1 Preparation of ultra-light PCF

Raw materials (DB) were purchased from the local market. The samples were washed with deionized water to remove surface impurities and then thoroughly dried in an oven at 60°C to remove absorbed moisture. The dried balloon flowers were then heated to the target temperatures (400°C, 500°C, 600°C, 700°C, 800°C, 900°C) and held at a rate of 5°C/min for four h. After the system was decreased to room temperature, a black ultralight block sample was collected and noted as PCF-X (where X is the corresponding carbonation temperature).

2.2 Characterization

Thermogravimetric analysis (TGA) of the samples was carried out in an argon atmosphere with a heating rate of 5°C/min. The morphology and pore structure of the PCF samples were recorded by scanning electron microscopy (SEM, Hitachi S-4800). The phase composition of the products was studied by Rigaku D/max-2400 powder x-ray diffractometer (XRD). The chemical bonding and surface states of each PCF sample were analyzed by x-ray photoelectron spectroscopy (XPS, ESCALAB 250XI). Fourier transform infrared spectroscopy (FT-IR, Nicolet) and Raman spectroscopy (Renishow 2000) were used to

detect the phase composition of the products. The prepared PCF samples were homogeneously mixed with paraffin wax at a mass ratio of 1:9. They were pressed into small circular rings with an inner diameter of 3 mm, an outer diameter of 7 mm, and a thickness of 3.04 mm. Then the electromagnetic parameters in the frequency range of 2 ~ 18 GHz were measured on an Agilent N5230A vector network analyzer.

3 Results And Discussion

Figure S1 exhibits the macroscopic photo of the DB and typical PCF foam, it changes from initial yellowish brown to dark black after the calcination treatment. As shown in Fig. 1a, the PCF foam is light enough to stand easily on a typical dogwood compared to the bulk carbon material. When plugging the DB and PCF foam into water (as shown in Fig. 1b), the former sank to the bottom while the latter floated on the surface. It is found that the density of the samples decreased sharply via an exclusive calcination treatment, and the density of the resulting product decreased gradually with increasing temperature (Fig. 1c); meanwhile, the circumference (perimeter) of the products displays an increasing tendency (Fig. 1d). Obviously, the corresponding density is reduced sharply by two orders of magnitude from 1.157 g/cm^3 of DB sample to 0.0254 g/cm^3 of the PCF-900 sample. Figure 1e exhibits the TGA-DTG curve of the DB sample. It can be observed that the mass loss is very tiny (only 4.41%) below 75 degrees Celsius (°C), which can be attributed to the decomposition of residual adsorbed water in the raw material [27]. Within the temperature range from 75°C to 265°C, a sharp mass loss with a ratio of 35.73% occurs, which can be assigned to the decomposition of cellulose and hemicellulose. At this stage, the macromolecular components are broken down into glucose, accompanied by the formation of water, which is released as a gas at this temperature. Another noticeable mass variation (about 17.4%) appears between 265°C and 375°C, which may be aroused by the further decomposition reaction of the obtained glucose, and different kinds of alcohols and acids can be further obtained. Meanwhile, some gaseous small molecule products, such as CO, CO_2, and CH_4, are released. When the calcination temperature is above 375°C, the mass variation curve of the DB is moderate, which more likely corresponds to the destruction of the structure of lignin in raw material [28]. At high temperatures (> 450 °C), the polycondensation reaction occurs quickly, the structure conversion of the polycyclic aromatic hydrocarbons occurs, and the derived carbon is subsequently collected. Figure 1f exhibits the XRD patterns of DB and various PCF samples obtained at different calcination temperatures. For DB, the diffraction peak that appeared at 16° can be assigned to the character of cellulose and hemicellulose. For various PCF foams, the broad diffraction peak around 23° can be assigned to (002) crystal plane of carbon [29], and the overall shape of the diffraction peak reveals the amorphous state and disordered characteristics of the product. It can be speculated that the DB has been converted into derived carbon products above 400°C, which is lower than the calcination temperature of other biomass-derived carbon. It is well known that the stems of herbaceous plants are mainly composed of cellulose, hemicellulose, and lignin. As shown in Fig. 1g, cellulose and hemicellulose have poor thermal stability, which can occur decomposition reactions at low temperatures, while the main component of lignin is a phenylpropane-based polymer, which has significantly higher thermal stability than cellulose and hemicellulose. As the

calcination temperature increases, the hydroxyl (-OH) originated from the glucose structure unit of cellulose easily converts to H_2O. Meanwhile, CO and CO_2 are generated from the glycoside bond (C-O-C) through a dehydroxylation reaction, and hemicellulose's xylose structure unit undergoes a degradation reaction, resulting in small molecule releases. The hydroxyl and methoxy groups on the phenylpropyl structural unit of lignin are easily separated from H_2O and CH_4. Overall, the organic matter from dried balloonflower pyrolyzes and evaporates completely after calcination treatment.

To exclude the interference of the difference of composition and carbonization degree, and to investigate the effect of morphology (hole size) on the microwave absorption performance of PCF, we prepared the PCF sample captured from horizontal and vertical cutting directions (as indicated in Fig. 2g & 2h), respectively. Figure 2a-f exhibit the SEM images of the fracture surface of various PCF samples collected from the horizontal direction. It is found that the PCF sample's cross-section is honeycomb-shaped, divided into dense prisms with diverse sizes and irregular shapes along the axial direction, which is different from DB. It can be confirmed that the pore size can be adjusted with increasing calcination temperatures, that is, the higher the temperature, the larger the pore size, which is consistent with the variation tendency of perimeter and density of PCF samples. Figure 2i-n shows the vertical section of the PCF samples, which also presents an irregular prismatic structure. Furthermore, the hole size of each sample is slightly larger than that of the cross-sectional sample. Generally, the porous material can be regarded as a complex composed of solid material and air interspersed with it. Therefore, the pore structure has an important influence on the absorption properties of porous absorbing material. Different sections of the PCF sample may achieve different electromagnetic wave attenuation capacities. Figure S2a displays the typical SEM image of DB captured from the horizontal section. It is found that the fracture surface is smooth with randomly distributed texture patterns appearing in the field of vision, which is composed of numerous primary cellulose. Figure S2b exhibits the SEM image of DB captured from the vertical section. Compared with Fig. S2a, the fracture surface of DB is rough with a more robust and bulky venation microstructure. It is inferred that this phenomenon may be related to the distribution direction of cellulose in the interior. Figure 2o-q reveal the element mapping collected from a typical PCF sample, and C, N, and O atoms can be detected obviously. The abundant C element suggests that the central part of the PCF is carbon, and the N and O elements uniformly distribute in carbon structure to form heterogeneous doping atoms. The doping atoms not only improve the conductivity and conduction loss, but also generate additional dipole polarization loss acting as polarization centers and exerting a positive effect on the dissipation of electromagnetic waves. To intuitively analyze the hole size variation, the statistical results of hole size distribution captured from the horizontal section and vertical sections were exhibited in Fig. S3a-f. Obviously, the hole size in a vertical section is more significant than that of the horizontal section obtained at the same temperature, suggesting that the microstructure of PCF sample can be successfully adjusted by changing the calcination temperature and cutting direction.

FT-IR spectra were employed to investigate the surface functional group information of various PCF samples, and the corresponding characterization results are shown in Fig. 3a. With the increase of calcination temperature, the FT-IR spectra of PCF samples gradually exhibit a flat variation tendency,

suggesting that some functional groups of the derived carbon were degraded dramatically, and the absorbance intensity decreased significantly. Figure 3b-d displays the partially enlarged drawing captured from the corresponding region of Fig. 3a, and several character absorption peaks can be recognized. In Fig. 3b, the absorption peak located around 580 cm^{-1} can be attributed to the stretching vibration of the C-H bond. It can be found that the relative intensity of the C-H bond does not vary with the calcination temperature of PCF samples. In Fig. 3c, the characteristic peak located at 1045 cm^{-1}, 1570 cm^{-1}, and 1630 cm^{-1} can be assigned to the stretching vibration of C-O bond in phenolic, alcohols, and ethers components, C = C bond or stretching vibration of the benzene ring skeleton, stretching vibrations of C-N, respectively. Notably, the integral area of the C-O absorption peak gradually decreases, meanwhile, its location shows a slight blue shift, indicating that the changes of microstructure depended on the calcination temperature. The relative intensity of the C-N characteristic peak also gradually decreases, which disappears in PCF-700 ~ PCF-900 samples, suggesting that some nitrogenous-containing functional groups cannot exist stably at high temperatures. Meanwhile, the relative intensity of the C = C characteristic peak increase with the increase of calcination temperature. In Fig. 3d, the characteristic peaks appearing at 2850 cm^{-1} and 2920 cm^{-1} can be attributed to the stretching vibration of -CH_3 and -CH_2 [30] from alkanes. Although their relative intensity decreases gradually, the corresponding integral area's ratio remains constant.

Figure 3e presents the Raman spectra of the PCF samples, in which two prominent peaks marked as D band and G band appear around 1300 cm^{-1} and 1580 cm^{-1}, respectively, corresponding to the characteristic peaks of carbon material. It is well known that the D peak represents the vibration of sp^3 atoms in disordered graphite [31], and the G peak stands for the in-plane vibration of sp^2 atoms in the two-dimensional hexagonal lattice [32].

The I_D/I_G value (the relative intensity ratio between the D band and the G band) is usually employed to evaluate the graphitization degree or disorder of carbon materials [33]. With the enhancement of calcination temperature, the I_D/I_G value of the PCF samples shows an increasing trend from 0.72 for PCF-400 to 0.96 for PCF-900. It should be noted that a higher calcination temperature is favorable to enhancing the graphitization degree of carbon-based material. In other words, the PCF-900 sample has a higher graphitization degree than the PCF-700 sample. Therefore, excluding the influence of graphitization degree, the higher I_D/I_G value of PCF-900 can be attributed to its more disordered lattice structure, which is consistent with the reduced trend of C-N and C-O bonds. These lattice defects can be served as polarization centers and generate abundant dipole polarization to enhance the absorption capacity of incident electromagnetic waves. Figure 3f shows the full-scan XPS spectra of obtained various PCF samples, and three characteristic peaks of C1s, O1s, and N1s can be detected at 285eV, 400eV, and 532eV, respectively. The content variation of each element in PCF samples was exhibited in Fig. 3g.

The main body of the skeleton is composed of carbon, which increases gradually with the increase of carbonization temperature. At the same time, the content of O and N elements decreases, suggesting that

the chemical composition of the PCF sample obtained can be perfectly adjusted by changing the pyrolysis temperature. Figure 3h-j shows the high-resolution N1s, C1s, and O 1s spectra of various PCF samples[34]. As exhibited in Fig. 3h, three peaks at 395.2eV, 397.6eV, and 403eV can be stripped from N1s spectra, representing pyridine-N, pyrrolic-N, and graphite-N, respectively [35]. With the increase of the carbonization temperature, both the relative intensity of the pyridine-N peak and the integrated area ratio of pyridinic-N to graphitic N gradually decreases, which is consistent with the change of C-N, C-O, and C = C bonds. The high-resolution C1s spectra of PCF samples obtained at different temperatures were shown in Fig. 3i, which can be divided into the following two peaks, C-C/C = C at 284.8 eV and C-N/C-O at 286.5 eV [36]. The integrated area ratio of the former to the latter gradually increases, indicating the enhanced order of graphite lattice. In addition, the peaks located at 527.8 eV and 530.5 eV (Fig. 3j) represent defective oxygen vacancy and surface-adsorbed oxygen, respectively. With the increase of carbonization temperature, the percentage of oxygen vacancy gradually increases.

The relative complex permittivity ($\varepsilon r = \varepsilon'-j\varepsilon''$) and the relative complex permeability ($\mu r = \mu'-j\mu''$) are the two key parameters that determine the absorption performances of microwaves [37]. The real part of the complex permittivity and complex permeability represents the ability of the absorbing material to store electromagnetic energy. In contrast, the imaginary part represents the ability of the absorbing material to lose electromagnetic energy. Since PCF samples are non-magnetic, their wave absorption properties are mainly determined by the permittivity, that is, the real and imaginary parts of permeability are 1 and 0, respectively. Figure 4a & b show the real part and imaginary part curves of the permittivity taken from each sample in the horizontal cutting directions, respectively. It can be seen from the plots that the values of both the real part and imaginary parts of the samples increase significantly with the increase of the calcination temperature, suggesting that the PCF samples obtained at high temperature possess the strongest energy storage capacity for electric filed. In the frequency range of 2 ~ 18 GHz, the real part values of the permeability for PCF-400H, PCF-500H, PCF-600H, and PCF-700H samples remain largely unchanged. The subtle difference of ε' values among them is closely related to their similar microstructure and surface-adsorbed functional groups. In Fig. 4b, the ε'' values of PCF-400H, PCF-500H, PCF-600H, and PCF-700H samples basically remained around 0 without fluctuation, which is an order of magnitude lower than corresponding ε' values, indicating that these samples can be regarded as wave-transparent materials with poor attenuation capacity for electromagnetic waves [38]. The real and imaginary parts of the PCF-800H sample show small fluctuations in the range of 12.1GHz to 18GHz, and 9.6GHz to 189.6GHz, respectively, which can be assigned to the resonance peak related to the better carbon network structure and good electrical conductivity. For the PCF-900H sample, the real part values gradually decrease from 13 at 2 GHz to 6.6 at 18 GHz, and the imaginary part values of 4.3 at 4 GHz increase gradually to 4.8 at 18 GHz, and both of them display multiple fluctuations at higher frequencies.

Figure 4c & d show the real and imaginary curves of the permeability for the vertical samples, respectively. Similar to the curves for each horizontal cutting sample, the values of the real and imaginary parts for each vertical cutting PCF sample also increase significantly with increasing reaction temperature. In the frequency range from 2 to 18 GHz, the real part values of the PCF-400V, PCF-500V, PCF-600V, and PCF-700V samples remain constant around 4.5, and their imaginary part values locate at

1.2 respectively. The real part values of the PCF-800V sample gradually decrease from 9.7 at 2GHz to 5.2 at 18GHz. The imaginary part value is 2.8 near 2GHz and gradually increases to 4.2 at 18GHz. For the PCF-900V sample, the real part values gradually decrease from 16.7 at 2GHz to 6.6 at 18GHz, meanwhile, its imaginary part value also decreases from 2.9 at 2GHz to 4 at 18GHz. Noteworthily, the imaginary part values of the PCF-900V are more significant than that of the PCF-900H, indicating its more robust attenuation capability for the electromagnetic wave. Furthermore, both the PCF-900H and PCF-900V display the synchronous change in S and C bands and achieve maximum value in Ku band and X band respectively, which is attributed to the dielectric polarization relaxation behavior, and suggesting their good dissipation capacity for electrical field energy. Figure 4e and Fig. 4f exhibit the dielectric loss tangent (tanδ) curves of PCF-900H and PCF-900V, in which the samples achieve higher tanδ values than other samples (especially in Ku band), which is consistent with the variation of ε" curves, revealing their good dielectric loss.

The reflection loss (RL) is usually used to evaluate the microwave absorption properties of the absorbing material. According to transmission line theory [39], the RL curve can be described as

$$\mathrm{RL}\,(\mathrm{dB}) = 20\log\left|\frac{Z_{\mathrm{in}} - Z_0}{Z_{\mathrm{in}} + Z_0}\right|$$

$$Z_{\mathrm{in}} = Z_0\sqrt{\frac{\mu_r}{\epsilon_r}}\tanh\left(\mathrm{j}\frac{2\pi \mathrm{fd}}{\mathrm{c}}\sqrt{\mu_r\epsilon_r}\right)$$

in above equations, Z_0 is the air impedance, Z_{in} stands for the input impedance, f represents the frequency, d is the sample thickness, c is the speed of light, ϵ_r and μ_r are the relative complex permittivity and magnetic permeability, respectively. In addition, effective absorption bandwidth (EAB) is generally employed to measure the frequency coverage range of the absorber for incident electromagnetic wave. Figure S4 (a-f) and Fig. S5 (a-f) show the $RL_{\min}$ plots versus thickness and frequency of the horizontal cutting PCF samples prepared at different calcination temperatures, respectively. The $RL_{\min}$ values of the PCF samples increase gradually with the increasing of the calciantion temperature. However, the $RL_{\min}$ values of PCF-400H, PCF-500H and PCF-600H samples are less than − 10 dB, which does not meet the requirements of EAB. It is almost certain that their poor microwave absorption performances is aroused by their weak imaginary part values of permittivity and poor dielectric loss capacity. For the PCF-700H, the EAB value is also small, and the optimal $RL_{\min}$ of -15.74 dB can be achieved at 5.5 mm matching thickness. When the calcination temperature reaches to 800°C, the PCF-800H displays the minimal RL value of -12.18 dB at 2.2 mm thickness, meanwhile, its EAB of 2.4 GHz is also measured at 2.36 mm thickness. Figure S4f, Fig. S5f and Fig. 5b exhibit the $RL_{\min}$ values of PCF-900H. As seen from these figures, the location appearing $RL_{\min}$ values gradually shift to low frequencies with the increase of the thickness, the $RL_{\min}$ of -24.65 dB is obtained when the matching thickness is 1.57 mm, while the widest EAB reaches to 6.24 GHz (11.76 GHz ~ 18 GHz) at 1.86 mm, covering the whole Ku band. Figure S5 and Fig. 5a show the RL relationship of various PCF samples versus frequency and matching thickness captured from the vertical cutting direction respectively. It is obvious that the $RL_{\min}$ values of the vertical

cutting PCF samples gradually increase, when the calcination temperature is higher than 600°C, the EAB values (<-10 dB) can be recognized. As shown in Fig. S4f, Fig. S5f and Fig. 5c, the PCF-900V exhibits outstanding electromagnetic wave absorption performances with the the minimum RL value of -46.95 dB at a thin thickness of 1.46 mm, meanwhile, and its optimal EAB value of 5.52GHz is achieved at 1.72mm thickness, indicating its good microwave absorption performance. The measurement results of different PCF samples were summarized, as exhibited in Fig. 5d. It can be clearly found that the RL_{min} and EAB values PCF-800 and PCF-900 samples is larger than that of PCF-400 ~ PCF-700, suggesting that higher calcination temperature is beneficial to obtain better absorption performances, which may be related to the structure integrity of carbon skeleton and conductivity of the as-synthesized product. Generally, the RL_{min} values of vertical cutting PCF samples with large hole size is better than that of horizontal cutting PCF samples, suggesting that the larger the hole size, the greater the reflection loss capacity, which is consistent with the results of Fig. 4b & c.

In order to evaluate the microwave absorption performance of PCF-900H and PCF-900V more intuitively, the two samples were compared systematically from the perspective of reflection loss, effective absorption bandwidth, matching thickness and location frequency, and the corresponding radar graph was shown in Fig. 5e. Obviously, the area enclosed by the irregular closed loop corresponding to PCF-900V sample is obviously larger than PCF-900H, suggesting that the comprehensive absorption properties of the former is better than later. Figure 5f and Tab. S1 exhibit the comparison of electromagnetic wave absorption performance of the PCF-900V with other materials, the result shows that the PCF-900V has a wider EAB with excellent RL_{min} value, which is in line with the characteristics of "thin, wide, light and strong" absorbing materials.

According to Debye theory [40], ε' and ε" can be expressed as

in which, ϵ_s, ϵ_∞, f, ϵ_0 and τ stand for static dielectric constant, optical dielectric constant, frequency, vacuum dielectric constant and polarization relaxation time, respectively. The dielectric relaxation can be evaluated by the following Cole-Cole equation:

$$\left(\epsilon' - \frac{\epsilon_s + \epsilon_\infty}{2}\right)^2 + \left(\epsilon''\right)^2 = \left(\frac{\epsilon_s - \epsilon_\infty}{2}\right)^2$$

A polarization relaxation process, can be reflected by a semicircle in Cole-Cole curve [41]. It is well known that the adhered adsorption functional groups on the porous carbon framework and the abundant O and N doping atoms on the carbon framework act as polarization centers, generating intense polarization relaxation and dielectric loss. As shown in Fig. S6 and Fig. 6a & b, the semicircles can be marked out, and the PCF-900H and PCF-900V samples achieve more semicircles quantity than other samples, which mainly occurs in X band and Ku band, suggesting their more polarization relaxation processes in these frequency range, which plays a significant role in enhancing the attenuation capacity of absorbing material [42, 43]. Moreover, the PCF-900H has the same number of semicircles as PCF-900V, and their relaxation phenomena are mainly concentrated in the Ku band. Attenuation coefficient and impedance

matching and are two crucial indexes to investigate the microwave absorption performance [44]. Figure 6c & d shows the attenuation constant of the PCF samples from horizontal and vertical cutting directions, respectively. Obviously, the attenuation constant values display the similar variation tendency with the curve of complex permittivity, indicating that the dielectric loss occupies a dominate position in determining the electromagnetic waves absorption properties. Compared with other samples, PCF-900H and PCF-900V achieve approximate maximum values in Ku band and strong microwave attenuation capacity in this frequency range. More importantly, it also implies that the different microwave absorption performances of horizontal and vertical cutting samples are almost negligibly affected by the attenuation coefficient. The impedance matching represents the capacity of the incident electromagnetic wave introduced into the absorber [45], which can be calculated by the Z_{in} value. Ideal impedance matching condition can be obtained while the value of $|Z_{in}\text{-}1|$ infinitely approaches 0 [46], indicating that all of the incident electromagnetic wave enters the sample ultimately. Figure 6e & f and Fig. S7 show the impedance matching plots of various PCF samples captured from horizontal cutting and vertical cutting, respectively. It can be seen that the impedance matching values of the PCF-900V and PCF-900V are closer to 1 than other samples in the frequency range of 2 ~ 18 GHz at the preferred thickness of themselves, which is more favorable to the absorption of electromagnetic waves. It should be noted that the plots of impedance matching versus thickness versus frequency for the above two samples are consistent with the plots of reflection loss variation (Fig. 5a & b), implying that the reflection loss performances of PCF-900H and PCF-900V are highly influenced by impedance matching.

On the basis of the above measured results, the attenuation process and working mechanism of the PCF sample on the incident electromagnetic waves are demonstrated, the corresponding schematic diagram was shown in Fig. 7. Firstly, as a typical derived carbon material, the PCF sample maintains the good electrical conductivity common to other carbon family members, which can produce some conductive loss under the action of the applied electromagnetic field. Secondly, the peculiar honeycomb structure of the PCF contains a large number of three-dimensional cavities, which arouses multiple reflection and scattering effects on the incident electromagnetic wave, and improves the impedance matching at the same time. Thirdly, the rich nitrogen, oxygen and other exotic atoms from the DB raw material are inherited by the PCF sample, who act as polarization centers together with a large number of dangling bonds or functional groups adsorbed on the surface, which produce strong dipole polarization loss to the incident electromagnetic waves and further weaken the energy of electromagnetic waves.

4 Conclusion

In this work, an ultra-light porous carbon foam was prepared through a simple calcination process without the introduction of activating agent. The characterization results indicate that the hole size and the content of hetero-atoms in the carbon skeleton depends largely on the carbonization temperature, which is significant for the electromagnetic wave dissipation. Remarkably, the cutting direction is another crucial factor for determining the performances of absorber, and the samples obtained along horizontal cutting direction are generally better than the ones from vertical cutting direction. For the optimal PCF-

900V, the minimum RL reaches to -46.95 dB at the thickness of 1.46 mm, and the effective absorption bandwidth of 5.52GHz is achieved at 1.72mm thickness. According to systematic characterization results, the electromagnetic wave absorption properties of the PCF samples should be attributed to conduction loss, interface polarization and hetero-atom induced dipole polarization, efficient multiple reflection and scattering. It is believed that ultra light PCF can be used as a low-cost and environmentally friendly carbon-based absorber or carrier in future electromagnetic pollution area.

Declarations

Conflict of interest The authors declare no competing interests.

References

1. Bola J, Popli H, Stolley R, Liu H, Malissa H, Kwon O, Boehme C, Miller J (2021) Fabrication Method, Ferromagnetic Resonance Spectroscopy and Spintronics Devices Based on the Organic-Based Ferrimagnet Vanadium Tetracyanoethylene. Adv. Funct. Mater. 31:2100681

2. Wu H, Lan D, Li B, Zhang L, Fu Y., Zhang, Y, Xing H (2019) High-entropy alloy@air@Ni-NiO core-shell microspheres for electromagnetic absorption applications. Compos. B. Eng 356(6304):107524.1-107524.12

3. Lan D, Qin M, Liu J, Wu G, Zhang Y, Wu H (2019) Novel binary cobalt nickel oxide hollowed-out spheres for electromagnetic absorption applications. Chem. Eng. J 382:122797

4. Liu T, Cao M, Feng Y, Zhu Y, Cao M (2022) Green building materials lit up by electromagnetic absorption function. A review J Mater Sci Technol 112:329-344

5. Jiang B, Yang W, Bai, H, Wang C, Xu C, Li Z, Yan L, Zhang C, Wu N, Che S, Wang X, Li Y (2022) Facile fabrication of Fe/Fe_5C_2@N-doped porous carbon as an efficient microwave absorbent with strong and broadband absorption properties at an ultralow filler loading. Carbon 196:890-901

6. Zhou B, Li C, Zhou Y, Liu Z, Gao X, Wang X, Jiang L, Tian M, Zhou F, Jerrams S, Yu J (2022) A flexible dual-mode pressure sensor with ultra-high sensitivity based on BTO@MWCNTs core-shell nanofibers. Compos Sci Technol 224:109478

7. Cheng Y, Zhao Y, Zhao H, Lv H, Qi X, Cao J, Ji G, Du Y (2019) Engineering morphology configurations of hierarchical flower-like $MoSe_2$ spheres enable excellent low-frequency and selective microwave response properties. Chem. Eng. J 372:390-398

8. Li Y, Sun H, Zhang Y, Xu M, Shi S (2019) The three-dimensional heterostructure synthesis of ZnO/cellulosic fibers and its application for rubber composites. Compos Sci Technol 177:10-17

9. Wang X, Lu Y, Zhu T, Cheng S, Wang W (2020) $CoFe_2O_4$/N-doped reduced graphene oxide aerogels for high-performance microwave absorption. Chem. Eng. J. 388:124317

10. Han Y, Yuan Y, Zhu Y, Wang Q, Li L, Cao M (2022) Implantation of WSe_2 nanosheets into multi-walled carbon nanotubes for enhanced microwave absorption. J. Colloid Interface Sci. 609:746-754

11. Zhao L, Guo Y, Xie Y, Cheng T, Meng A, Yuan L, Zhao W, Sun C, Li Z, Zhang M (2022) Construction of SiCNWS@NiCo2O4@PANI 1D hierarchical nanocomposites toward high-efficiency microwave absorption. Appl. Surf. Sci. 592:153324

12. Li Z, Lin H, Xie Y, Zhao L, Guo Y, Cheng T, Ling H, Meng A, Li S, Zhang M (2022) Monodispersed Co@C nanoparticles anchored on reclaimed carbon black toward high-performance electromagnetic wave absorption. J Mater Sci Technol 124:182-192

13. Wen M, Zhao Y, Li Z, Lai S, Zeng Q, Liu C, Liu Y (2021) Preparation of lignin-based carbon/polyaniline composites for advanced microwave absorber. Diam Relat Mater 111:108219

14. Jia Z, Kou K, Yin S, Feng A, Zhang C, Liu X, Cao H, Wu G (2020) Magnetic Fe nanoparticle to decorate N dotted C as an exceptionally absorption-dominate electromagnetic shielding material. Compos. B. Eng. 189:107895

15. Zhang M, Lin H, Ding S, Wang T, Li Z, Meng A, Li Q, Lin Y (2019) Net-like SiC@C coaxial nanocable towards superior lightweight and broadband microwave absorber. Compos. B. Eng. 179:107525

16. Zhang M, Ling H, Wang T, Jiang Y, Song G, ZhaoW, Zhao L, Cheng T, Xie Y, Guo Y (2022) An Equivalent Substitute Strategy for Constructing 3D Ordered Porous Carbon Foams and Their Electromagnetic Attenuation Mechanism. Nanomicro Lett 14:157

17. Wang Y, Zhou W, Zeng G, Chen H, Lou H, Fan X, Li Y (2021) Rational design of multi-shell hollow carbon submicrospheres for high-performance microwave absorbers. Carbon 175:233-242

18. Li Z, Lin H, Wu S, Su X, Wang T, Zhao W, Jiang y, Ling H, Meng A, Zhang M (2020) Rice husk derived porous carbon embedded with Co3Fe7 nanoparticles towards microwave absorption. Compos Sci Technol 229:109673

19. Song G, Li Z, Meng A, Zhang M, Li K, Zhu K (2017) Large-scale template-free synthesis of N-doped graphene nanotubes and N-doped SiO2-coated graphene nanotubes: Growth mechanism and field-emission property. J. Alloys Compd. 706:147-155

20. Dong S, Tang W, Hu P, Zhao X, Zhang X, Han J, Hu P (2019) Achieving excellent electromagnetic wave absorption capabilities by construction of MnO nanorods on porous carbon composites derived from natural wood via a simple route. ACS Sustain. Chem. Eng 7(13):11795-11805

21. Zhang X, Dong Y, Pan F, Xiang Z, Zhu X, Lu W (2021) Electrostatic self-assembly construction of 2D MoS_2 wrapped hollow Fe_3O_4 nanoflowers@1D carbon tube hybrids for self-cleaning high-performance microwave absorbers. Carbon 177:332-343

22. Zhou X, Jia Z, Feng A, Wang X, Liu J, Zang M, Cao H, Wu G (2019) Synthesis of fish skin-derived 3D carbon foams with broadened bandwidth and excellent electromagnetic wave absorption performance. Carbon 152:827-836

23. Zhang D, Liu T, Cheng J, Chai J, Yang X, Wang H, Zheng G, Cao M (2019) Light-weight and low-cost electromagnetic wave absorbers with high performances based on biomass-derived reduced graphene oxides. Nanotechnology 30:445708

24. Zheng S, Zhang J, Deng H, Du Y, Shi X (2021) Chitin derived nitrogen-doped porous carbons with ultrahigh specific surface area and tailored hierarchical porosity for high performance supercapacitors. JB&B 6:142-151

25. Obey G, Adelaide M, Ramaraj R (2022) Biochar derived from non-customized matamba fruit shell as an adsorbent for wastewater treatment. JB&B 7:109-115

26. Li Z, Wang X, Ling H, Lin H, Wang T, Zhang M, Meng A, Li Q (2020) Electromagnetic wave absorption properties of SiC@ SiO2 nanoparticles fabricated by a catalyst-free precursor pyrolysis method. J. Alloys Compd. 830:154643

27. He L, Zhao P, Han Q, Wang X, Cai X, Shi Y, Zhou L, Zhang Y, Xue W (2013) Surface modification of poly-l-lactic acid fibrous scaffolds by a molecular-designed multi-walled carbon nanotube multilayer for enhancing cell interactions. Carbon 56:224-234

28. Yang G, Park S (2018) MnO_2 and biomass-derived 3d porous carbon composites electrodes for high performance supercapacitor applications. Journal of Alloys & Compounds 741:360-364

29. Zhao H, Cheng Y, Zhang Z, Zhang B, Pei C, Fan F, Ji G (2021) Biomass-derived graphene-like porous carbon nanosheets towards ultralight microwave absorption and excellent thermal infrared properties. Carbon 173:501-511

30. Liu Z, Li C, Zhang X, Zhou B, Wen S, Zhou Y, Chen S, Jiang L, Jerrams S, Zhou F (2022) Biodegradable Polyurethane Fiber-Based Strain Sensor with a Broad Sensing Range and High Sensitivity for Human Motion Monitoring. ACS Sustain. Chem. Eng. 10:8788-8798

31. Liu P, Gao S, Wang Y, Huang Y, He W, Huang W, Luo J (2019) Carbon nanocages with N-doped carbon inner shell and Co/N-doped carbon outer shell as electromagnetic wave absorption materials. Chem. Eng. J 381:122653

32. Zhu B, Lv D, Xu K, Chen Y, Wei Y, Wei H, Bu J (2020) Synthesis of setaria viridis-like TiN fibers for efficient broadband electromagnetic wave absorption in the whole X and Ku bands. Appl. Surf. Sci. 533:147439

33. Zhou X, Jia Z, Feng A, Wang K, Liu X, Chen L, Cao H, Wu G (2020) Dependency of tunable electromagnetic wave absorption performance on morphology-controlled 3D porous carbon fabricated by biomass. Compos. Commun. 21:100404

34. Zhao J, Wei Y, Zhang Y, Zhang Q (2022) 3D flower-like hollow CuS@PANI microspheres with superb X-band electromagnetic wave absorption. J Mater Sci Technol 126:141-151

35. Cai W, Wang C, Fang X, Yang L, Chen X (2015) Synthesis and characterization of nitrogen-doped graphene films using c5ncl5. Appl. Phys. Lett. 106:1308

36. Zhao G, Wang F, Liu M, Sui Y, Zhang Z, Kang F, Yang C (2022) A high-frequency flexible symmetric supercapacitor prepared by the laser-defocused ablation of MnO2 on a carbon cloth. NEW CARBON MATER 37:556-563

37. Liu P, Gao S, Wang Y, Zhou F, Huang Y, Luo J (2020) Metal-organic polymer coordination materials derived Co/N-doped porous carbon composites for frequency-selective microwave absorption. Compos. B. Eng. 202:108406

38. Yu X, Zhang Y, Wang L, Xing L, You W, Liu J, Chen G, Ding G, Ding J, Liu X, Wang M, Che R (2020) Improved microwave absorption performance of multi-dimensional Fe_2O_3/CNTCM@CN assembly by enhanced dielectric relaxation. J. Mater. Chem. C 8:5715-5726

39. Qin F, Brosseau C (2012) A review and analysis of microwave absorption in polymer composites filled with carbonaceous particles. J. Appl. Phys. 111:061301

40. Xu D, Qiao J, Wu N, Liu W, Wang F, Lv L, Pan J, Domg Y, Liu J (2019) Facile synthesis of three-dimensional porous Co/MnO composites derived from bimetal oxides for highly efficient electromagnetic wave absorption. ACS Sustain. Chem. Eng 7:8687-8695

41. Gao X, Jiu Z, Wang B, Wu X, Sun T, Liu X, Chi Q, Wu G (2021) Synthesis of NiCo-LDH/MXene hybrids with abundant heterojunction surfaces as a lightweight electromagnetic wave absorber Carbon 194:207-219

42. Lou Z, Yuan C, Zang Y, Li Y, Cai J, Yang L, Wang W, Han H, Zou J (2018) Synthesis of porous carbon matrix with inlaid Fe_3C/Fe_3O_4 micro-particles as an effective electromagnetic wave absorber from natural wood shavings. J. Alloys Compd. 775:800-809

43. Quan B, Liang X, Ji G, Cheng Y, Liu W, Ma J, Zhang Y, Li D, Xu G (2017) Dielectric polarization in electromagnetic wave absorption. J. Alloys Compd. 728:1065-1075

44. Ye X, Chen Z, Zhang J, Wu C, Zhou Q, Ai S, Liu H, Cui S (2019) Double network nested foam composites with tunable electromagnetic wave absorption performances. Inorg. Chem. Front. 6:1579-1586

45. Xu H, Yin X, Zhu M, Han M, Hou Z, Li X, Zhang L, Chang L (2017) Carbon hollow microspheres with a designable mesoporous shell for high performance electromagnetic wave absorption. ACS Appl. Mater. Interfaces 9:6332-6341

46. Ye X, Chen Z, Ai S, Hou B, Zhang J, Zhou Q, Liu H, Cui S (2019) Enhanced electromagnetic absorption properties of Novel 3D-CF/PyC modified by reticulated sic coating. ACS Sustain. Chem. Eng 7:11386-11395
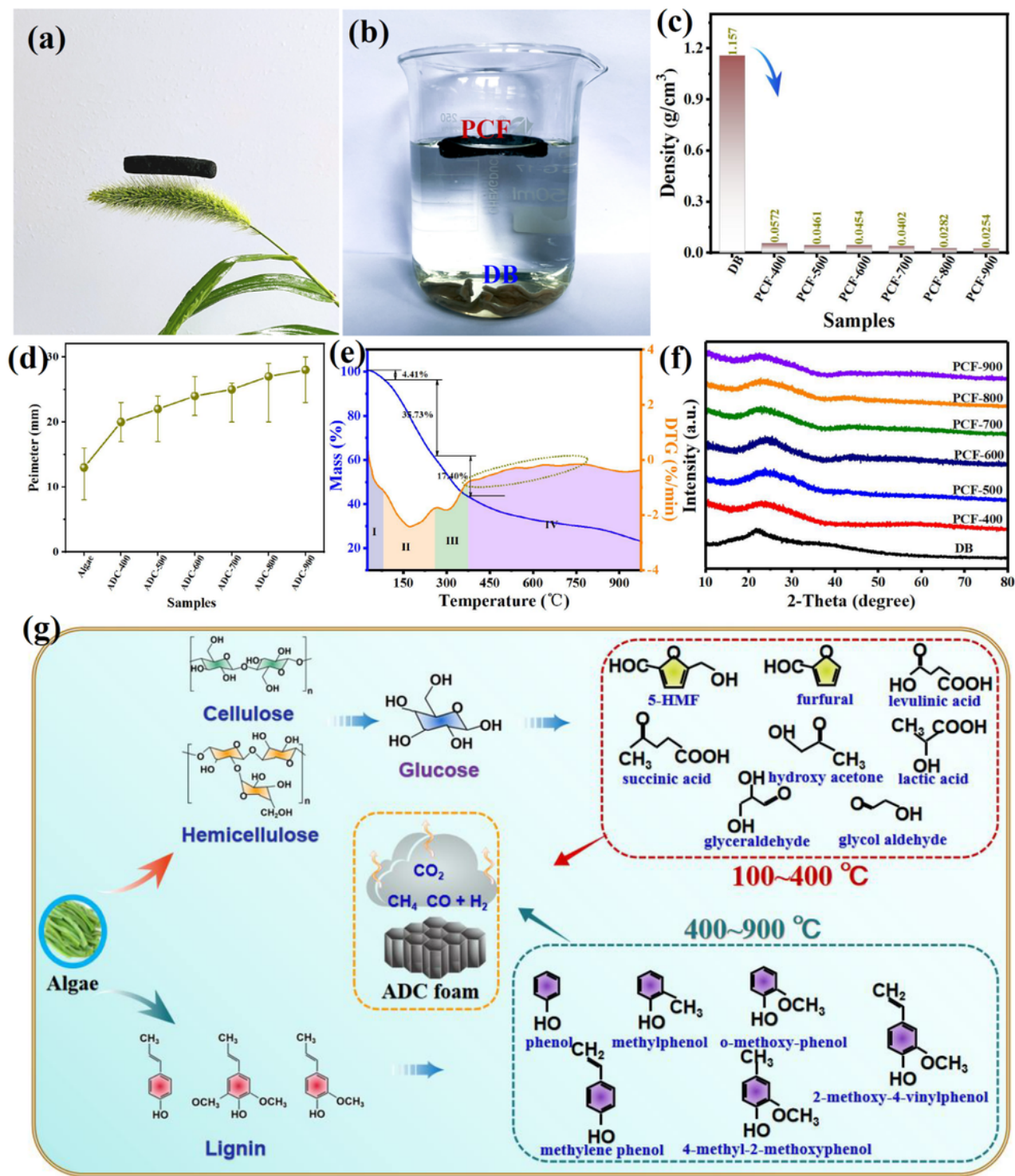
Figures

Figure 1

a PCF sample can easily stand on dogwood. **b** Macroscopic photograph of DB and PCF sample in water. **c** Density and **d** perimeter variation of DB and various PCF samples. **e** TGA-DTG variation curves of DB. **f**

XRD patterns of PCF samples prepared at different sintering temperature temperatures. **g** Schematic diagram of the compositional change process of DB
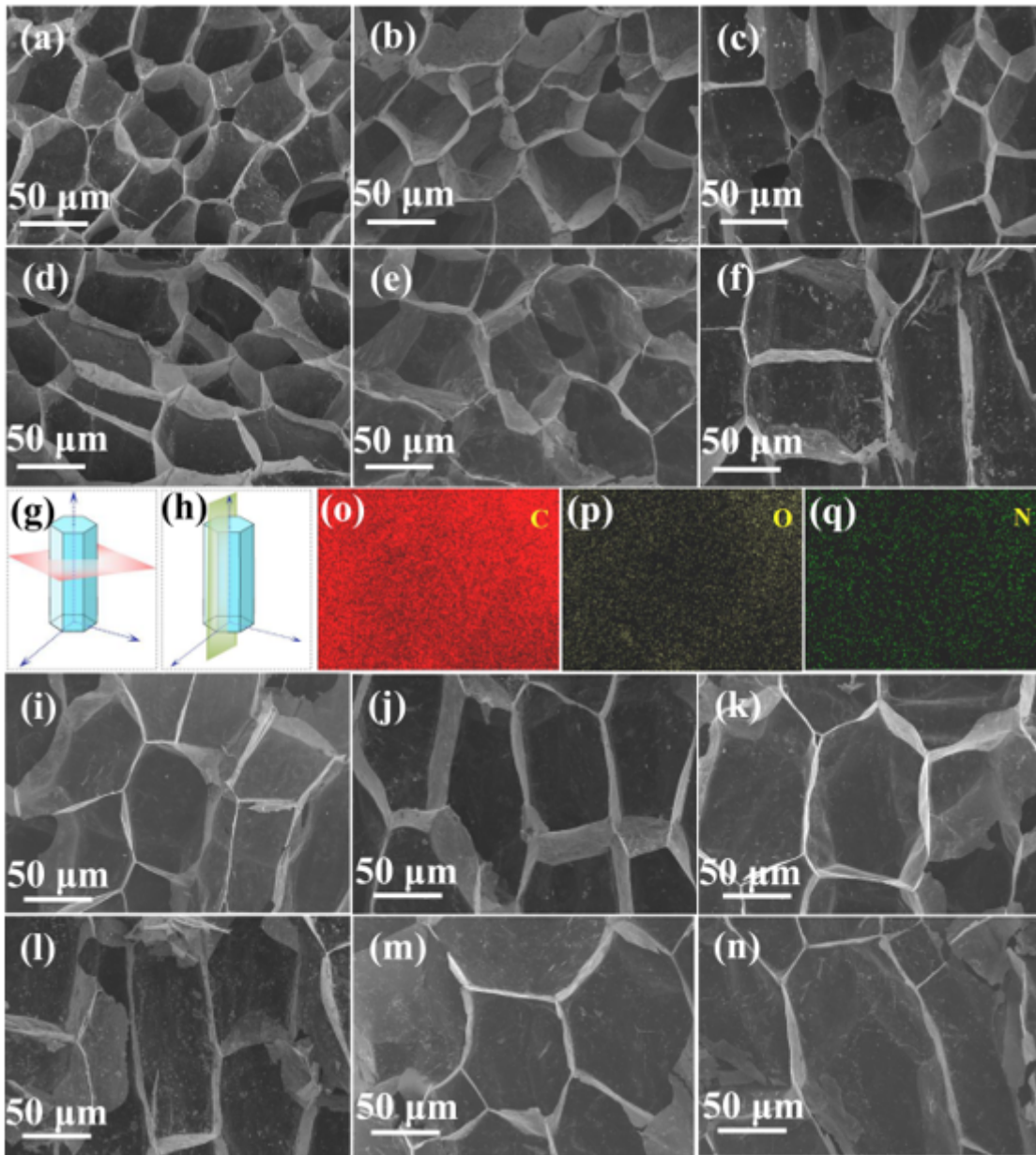

Figure 2

SEM images of various PCF samples captured from horizontal direction **a** PCF-400H, **b** PCF-500H, **c** PCF-600H, **d** PCF-700H, **e** PCF-800H, **f** PCF-900H. Schematic diagram of the horizontal section **g** and vertical section **h** of the PCF samples. SEM images of various PCF samples captured from vertical direction **a** PCF-400V, **b** PCF-500V, **c** PCF-600V, **d** PCF-700V, **e** PCF-800HV, **f** PCF-900V. Element mapping of C (**o**), O (**p**) and N (**q**) in the PCF sample.
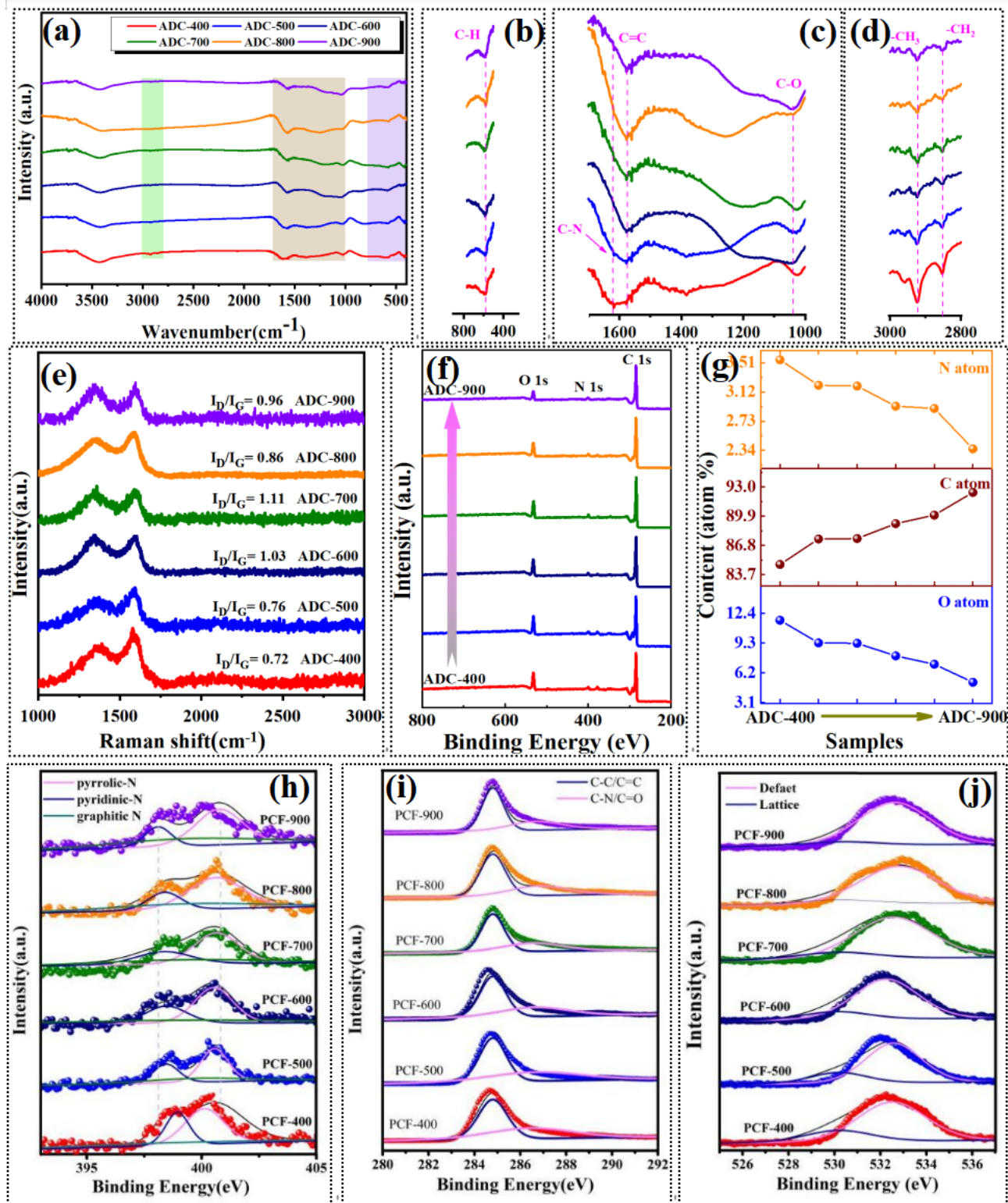
Figure 3

a FT-IR spectra of various PCF samples; **b-d** Partial enlarged images of the marked area in Fig. 3a; **e** Raman patterns of various PCF samples; **f** Full-scan XPS spectra of PCF samples; **g** Content variation of different elements in PCF samples; **h-j** High-resolution spectra N 1s, C 1s, and O 1s.
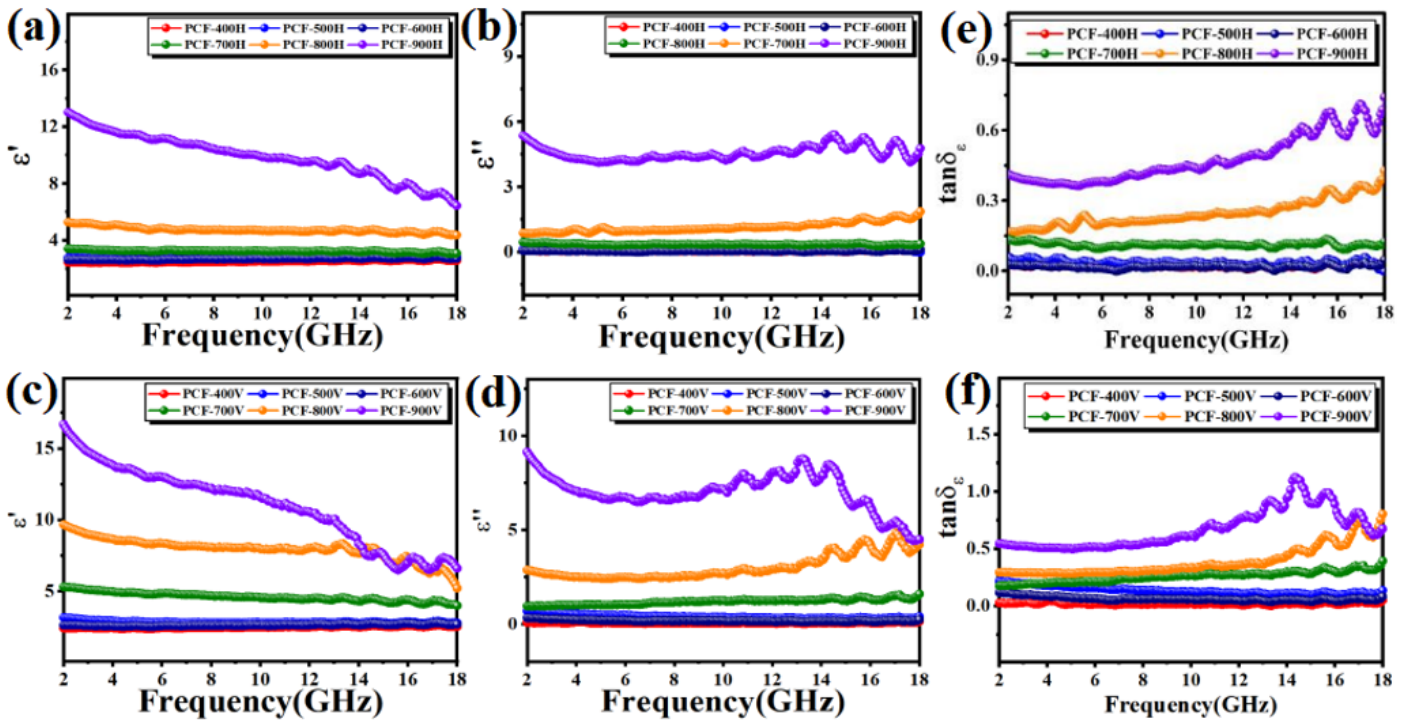
Figure 4

Real part (**a**, **d**) and imaginary part (**b**, **e**) of complex permittivity of the PCF samples. Dielectric loss tangent of various PCF samples (**c**, **f**).
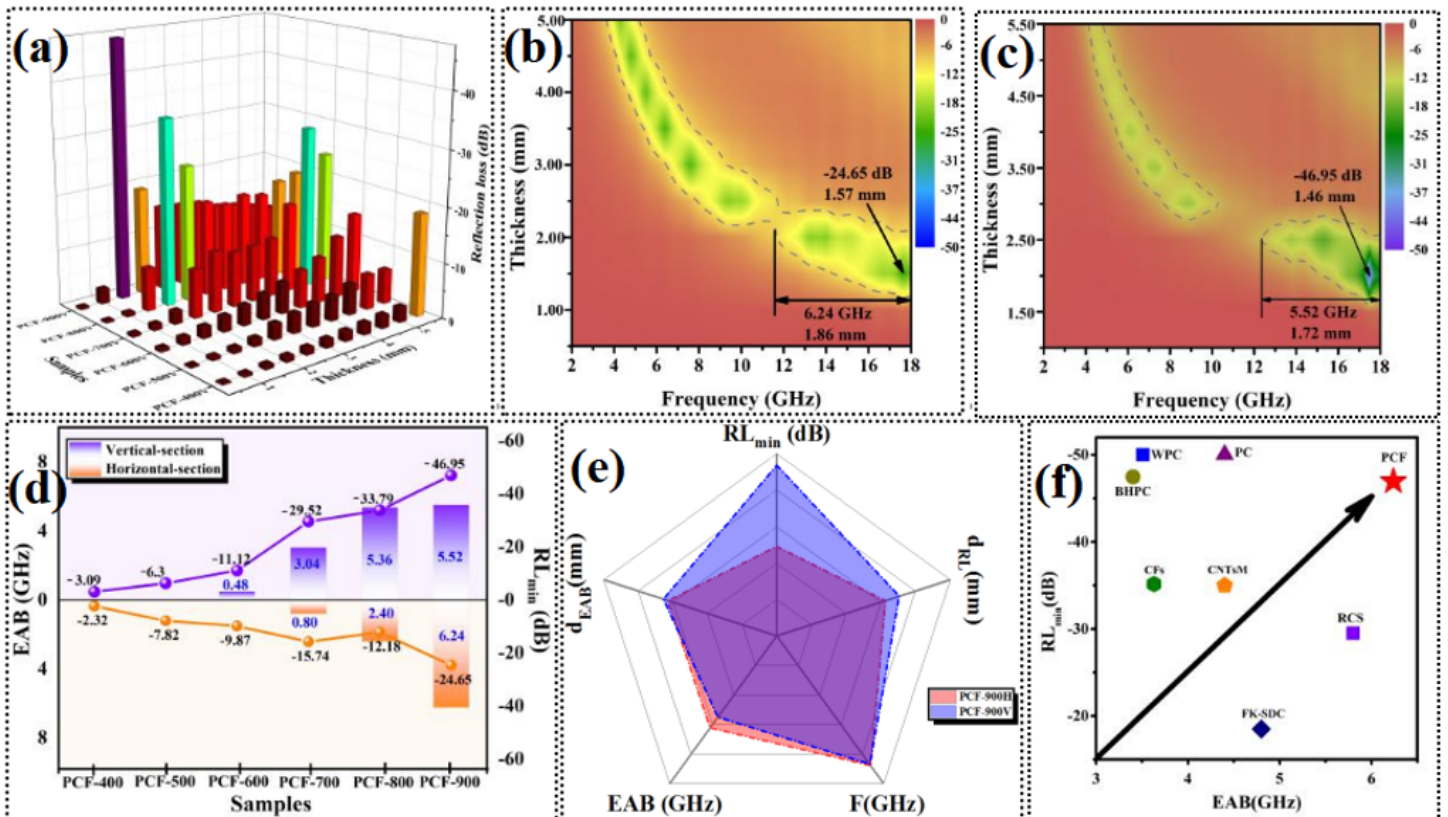
Figure 5

3D reflection loss value versus frequency and thickness of PCF-900H (**a**) and PCF-900V (**b**). **c** The optimal RL_{min} values of various vertical cutting PCF samples at different thickness. **d** Comparison of the preferred RL_{min} and EAB values of different PCF samples from the horizontal and vertical cutting directions. **e** Radar comparison chart of microwave absorption performances of PCF-900H and PCF-900V samples. **f** RL_{min} versus thickness of derived porous carbon absorbing material reported recently.
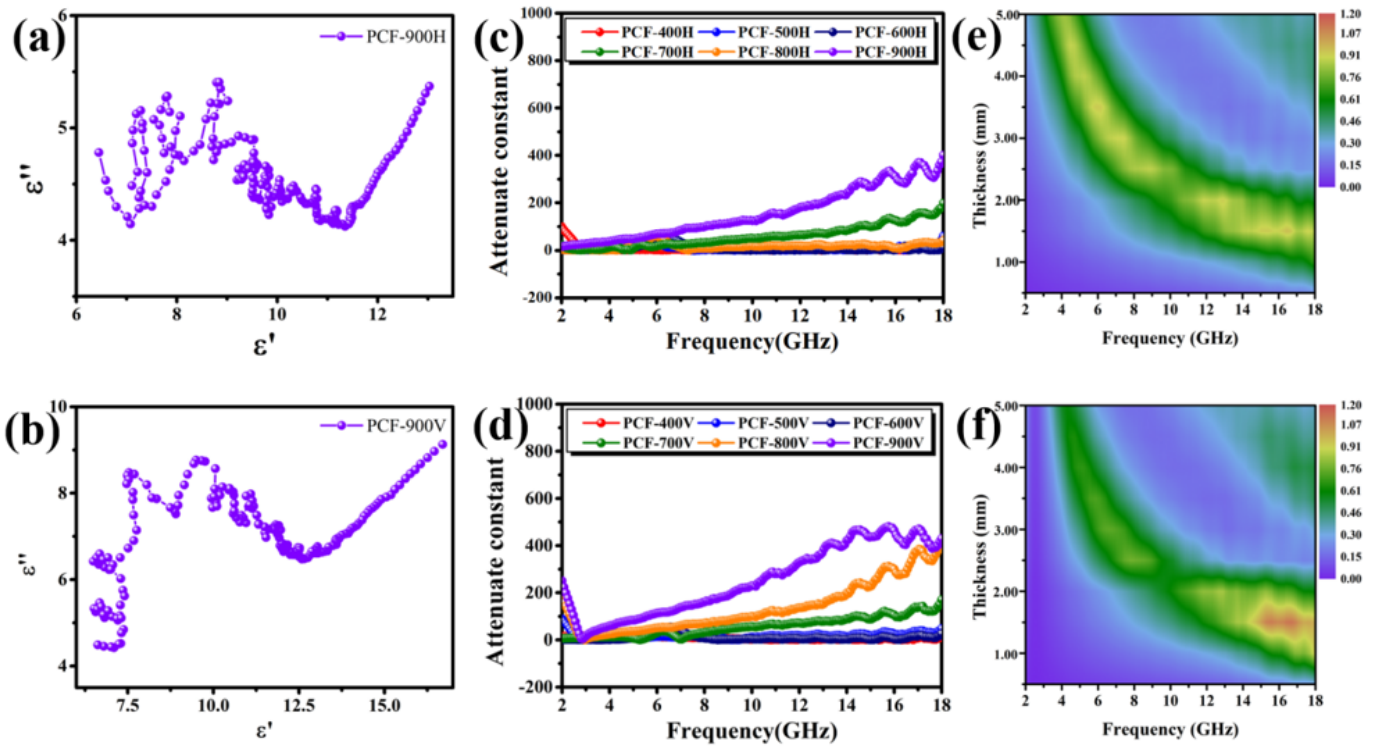
Figure 6

Cole-cole curve of PCF-900H (**a**) and PCF-900V (**b**). **c** & **d** The impedance matching of various PCF samples captured from the horizontal and cutting direction. **e** & **f** The attenuation constant of PCF-900H and PCF-900V.
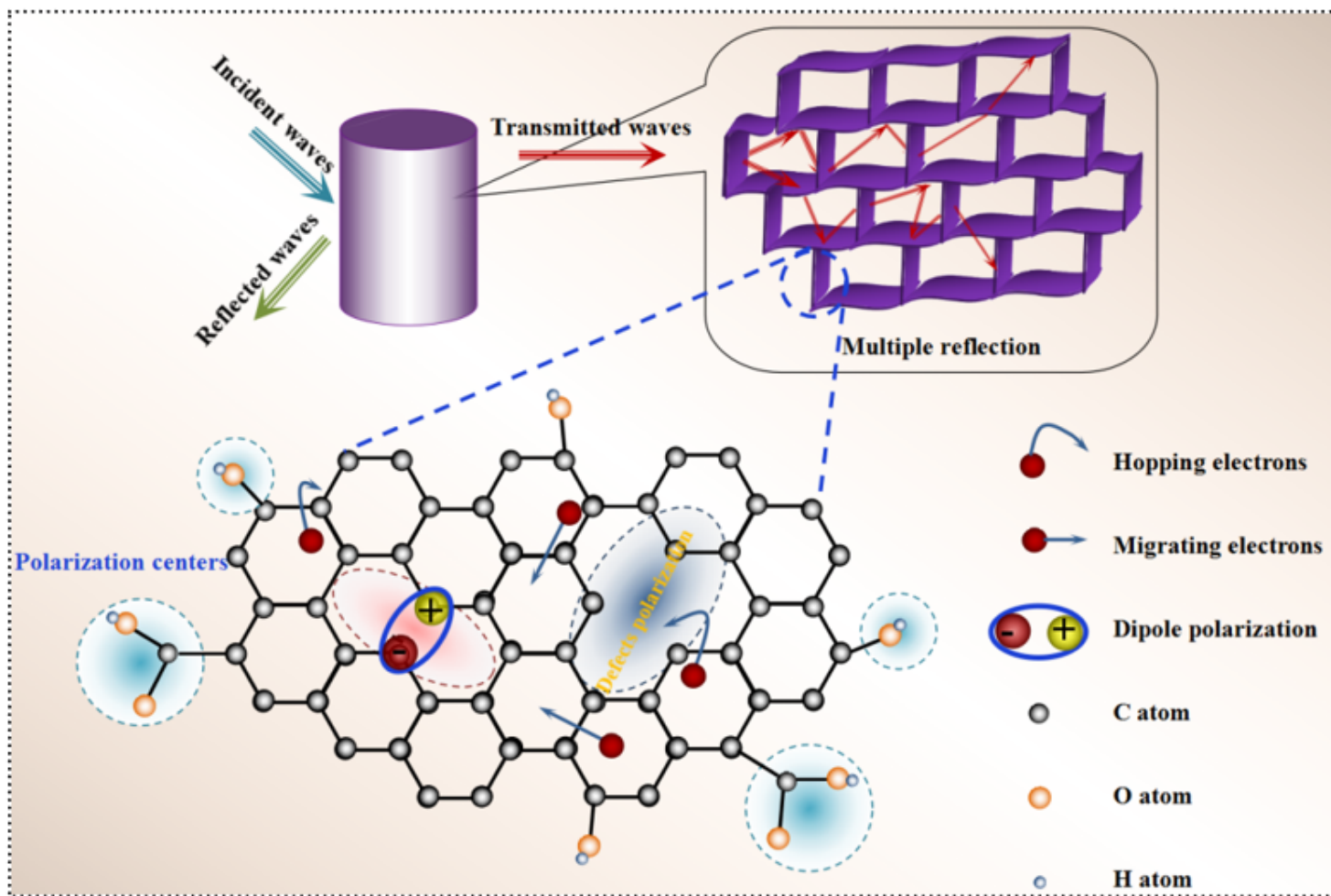
Figure 7

Schematic diagrams of the microwave absorption mechanism of the PCF sample.

Supplementary Files

This is a list of supplementary files associated with this preprint. Click to download.

- SupportingInformation.doc